

Characterizing the galactic gravitational wave background with LISASeth E. Timpano,^{*} Louis J. Rubbo,[†] and Neil J. Cornish*Department of Physics, Montana State University, Bozeman, Montana 59717, USA*

(Received 7 December 2005; published 2 June 2006)

We present a Monte Carlo simulation for the response of the Laser Interferometer Space Antenna (LISA) to the galactic gravitational wave background. The simulated data streams are used to estimate the number and type of binary systems that will be individually resolved in a 1-year power spectrum. We find that the background is highly non-Gaussian due to the presence of individual bright sources but, once these sources are identified and removed, the remaining signal is Gaussian. We also present a new estimate of the confusion noise caused by unresolved sources that improves on earlier estimates.

DOI: [10.1103/PhysRevD.73.122001](https://doi.org/10.1103/PhysRevD.73.122001)

PACS numbers: 04.80.Nn, 95.55.Ym

I. INTRODUCTION

Binary star systems are excellent sources of gravitational waves, and with roughly two-thirds of the $\sim 10^{11}$ stars in our galaxy in binary systems, there will be no shortage of targets for the proposed Laser Interferometer Space Antenna (LISA) [1]. Binaries with periods less than a day may potentially dominate the response of the LISA observatory. Indeed, it is likely that the main source of noise for LISA over a portion of its band will be unresolved gravitational wave signals from galactic and extragalactic binary star systems. Several studies [2–6] have sought to model these populations and estimate their contribution to the gravitational wave power spectrum. In some instances, these estimates have been combined with data analysis considerations to make predictions of the confusion noise caused by unresolved sources. Although a consensus has not formed on the expected background level, it is generally accepted that a galactic gravitational wave background does exist inside the LISA band. The difficulty in developing strong limits on the background level originates from the expectation that the background will be dictated by compact binaries, that is, binary systems that contain white dwarfs, neutron stars, and stellar mass black holes. Since the electromagnetic luminosity of compact binaries is low, not enough sources have been observed yet to build reliable models for the populations.

If current estimates of compact binary populations reasonably represent the true nature of the galaxy, then the superposition of gravitational wave signals from these populations will form a confusion limited background in the LISA band. That is, there will be enough sources that the received signals will interfere with each other to the point where individual binaries cannot be resolved [7]. When this occurs the background becomes a source of

noise in the detector. However, around ten thousand systems will be resolvable due to either their isolation in frequency space (for sources with frequencies above ~ 3 mHz) or their relative brightness (for sources below ~ 3 mHz).

Here we present a Monte Carlo model for the galactic gravitational wave background. Our goal is to better understand the role played by the rare, bright sources that dominate the observed signal, and to provide a more realistic level of the confusion background due to unresolved compact binaries. Our investigation of the galactic gravitational wave background is done in two phases. The first phase is to build a Monte Carlo simulation of the background by modeling each binary and processing the corresponding gravitational wave signal through a model of LISA. To reasonably represent the individual types of binaries, we follow the population models presented by Hils, Bender, and Webbink [3], and Nelemans, Yungelson, and Portegies Zwart [8], which from here on will be referred to as HBW and NYZ, respectively. Though less up to date, the HBW model has the advantage of being expressed in terms of explicit distribution functions, which allows us to generate multiple realizations. The more modern NYZ model employs a population synthesis code that has not been made public, so we were not able to generate our own realizations. Gils Nelemans was kind enough to send us a realization of the NYZ model to work with. The second phase of our study is to statistically characterize features of the galactic background as they are observed by LISA.

As part of the modeling phase, the signal from each source is run through a realistic model of the LISA instrument response to produce simulated interferometry data. In doing so, it was necessary to develop a new, fast algorithm for computing the detector response in order to process the $\sim 10^8$ sources modeled in each realization. The algorithm is based on the frequency domain approach developed by Cornish and Larson [9], and extended to include the detector transfer functions, arbitrary observation times, and frequency evolution of the sources. For the current study

^{*}Current address: Center for Gravitational Wave Physics, Pennsylvania State University, University Park, PA 16802.

[†]Current address: Center for Gravitational Wave Physics, Pennsylvania State University, University Park, PA 16802.

we set the observation time at $T_{\text{obs}} = 1$ year. Examples of our simulated LISA data streams can be found at the *Mock LISA Data Archive* [10].

Using the simulated detector data we investigate issues that are of importance to the development of future data analysis algorithms. Among the quantities we investigate are tests of Gaussianity in the distribution of Fourier coefficients before and after bright sources are removed, the number and type of bright sources, and the density (in frequency space) of bright sources. Our interest in bright systems stems from the idea that they will be identifiable in the data streams, and thus removable. They will also be instrumental in using the real gravitational wave data to study galactic populations and galaxy evolution.

To model the removal of bright systems we use an iterative procedure using a running median of co-added instrument noise and galactic signals as the effective noise level. Sources were considered bright if they had a signal noise ratio (SNR) greater than some threshold with respect to the effective noise level. We considered both optimistic (SNR = 5) and conservative (SNR = 10) thresholds. As the bright sources are regressed from the data, the effective noise level drops, allowing more sources to be resolved. After several iterations we are left with a residual signal that is our estimate of the galactic confusion noise. Previous estimates of the confusion noise were derived by setting a maximum source density, with the reasoning that it would be impossible to resolve individual sources when the number of sources per $1/T_{\text{obs}}$ frequency bin exceeded some threshold. Here we took a different approach that is based primarily on SNR thresholds, but we also studied the effect of a source density cutoff. Rather than working with the total source density we based our cutoff on the density of resolved sources. In other words, we considered the possibility that there will be a maximum number of sources that can be resolved per frequency bin. We studied the effect of a resolved source density cutoff by performing the iterative removals with and without a cutoff on the number of sources that could be resolved per frequency bin (we set a limit of one source per four bins). For some models the source density cutoff had a significant impact, but for other models the cutoff made very little difference. Our estimate of the confusion level for the HBW model differs from that of Bender and Hils [4] despite the fact that we use the same galactic model. Our estimate of the confusion level for the NYZ model agrees fairly well with Barack and Cutler [11] estimate. In both cases, our estimate is lower at low frequencies (below 1 or 2 mHz, respectively), and higher at high frequencies. The differences are due to our differing approaches to modeling the signal identification and regression. We feel that our approach yields more realistic estimates. All our examples are for one year of observations, so the frequency bins have width $\Delta f = 3.17 \times 10^{-8}$ Hz. The level of the confusion background will drop for longer observation times as the

sidebands get better resolved and the SNR increases. The reduction in the confusion noise over time means that fits to transient sources that occur in the first year of operation, such as a supermassive black hole merger, will continue to get better with time even though the source disappeared years ago.

Recently Benacquista *et al.* [12] and Edlund *et al.* [13] simulated LISA time series for a population of galactic white dwarf binaries. While comparable to our approach, neither simulation was used to study source identification and subtraction. The statistical analysis of the background given in Ref. [13] focuses on the cyclostationary nature of the signal, whereas our statistical analysis focuses on simulating data analysis in order to better understand the galactic gravitational wave background.

Since the study of the galactic gravitational wave background naturally divides itself into two sections, modeling and characterization, the outline of the paper follows suite. Sections II and III are devoted to a description of the Monte Carlo simulation of the galactic close binary populations. It is here that we describe how the individual sources are modeled and convolved with a LISA response model. The next three sections calculate a number of statistical properties associated with the galactic background. Section IV demonstrates that the galactic background is non-Gaussian in nature. In Sec. V we present our estimate of the confusion limited background and compare it to prior estimates. Section VI describes the characteristics of the systems that are labeled as bright. The paper concludes in Sec. VII with a discussion of the various assumptions used in the simulation and how changes in these assumptions may alter our results.

II. GALACTIC MODEL

The first step in building a Monte Carlo realization of the galaxy is to model an individual binary system. In general, a gravitational wave traveling in the \hat{k} direction can be decomposed into two polarization states,

$$\mathbf{h}(ct - \hat{k} \cdot \mathbf{x}) = h_+(ct - \hat{k} \cdot \mathbf{x})\epsilon^+ + h_\times(ct - \hat{k} \cdot \mathbf{x})\epsilon^\times, \quad (1)$$

where $\epsilon^{+,\times}$ are basis tensors used to describe the radiation's orientation. The scalar coefficients are referred to as the gravitational waveforms. For a circular binary with instantaneous angular orbital frequency Ω , and component mass M_1 and M_2 , the waveforms measured at the barycenter of the Solar System are

$$h_+(t) = A_+ \cos(2\psi) \cos(2\Omega t + \varphi_o) + A_\times \sin(2\psi) \sin(2\Omega t + \varphi_o) \quad (2a)$$

$$h_\times(t) = -A_+ \sin(2\psi) \cos(2\Omega t + \varphi_o) + A_\times \cos(2\psi) \sin(2\Omega t + \varphi_o), \quad (2b)$$

where the polarization amplitudes are given by

$$A_+ = \frac{2G^2 M_1 M_2}{c^4 r} \left(\frac{\Omega^2}{G(M_1 + M_2)} \right)^{1/3} (1 + \cos^2(\iota)) \quad (3a)$$

$$A_\times = -\frac{4G^2 M_1 M_2}{c^4 r} \left(\frac{\Omega^2}{G(M_1 + M_2)} \right)^{1/3} \cos(\iota). \quad (3b)$$

The angles ψ and ι describe the orientation of the binary as viewed by an observer in the barycenter frame, while φ_o is the initial phase.

Gravitational waves carry away energy and angular momentum from the emitting system. Consequently, a binary will slowly inspiral over time. For stellar mass galactic sources in the LISA band the period evolution can be adequately described by

$$P_{orb}(t) = \left(P_o^{8/3} - \frac{256}{5c^5} (2\pi)^{8/3} (G\mathcal{M})^{5/3} t \right)^{3/8}, \quad (4)$$

where $\mathcal{M} \equiv (M_1 M_2)^{3/5} (M_1 + M_2)^{-1/5}$ is the so-called chirp mass and P_o is the initial orbital period. Equation (4) does make the assumption, which is used throughout this paper, that no other processes (e.g. mass transfer) are evolved in the binary evolution besides gravitational wave emission.

Equations (2)–(4) indicate that a circular binary is uniquely determined by a set of nine parameters: the component masses (M_1, M_2), initial orbital period (P_o), binary orientation (ψ, ι), initial phase (φ_o), and the distance to the source (r). Additionally, two angular variables (θ, ϕ) are used to locate the source on the celestial sphere. To model an individual binary requires an accurate representation of these nine parameters.

The list of source parameters are separable into those that are extrinsic and intrinsic to the system. The extrinsic variables $\{r, \theta, \phi, \psi, \iota, \varphi_o\}$ do not influence the evolution of the binary. Instead they depend on the time of observation and on the location of the observer with respect to the binary. The remaining variables $\{M_1, M_2, P_o\}$ directly effect the binary evolution through the emission of gravitational waves via Eq. (4).

A. Extrinsic parameters

For the set of extrinsic variables there is a further separation into those that locate the source $\{r, \theta, \phi\}$ and those that describe the time of observation and orientation as viewed by a particular observer $\{\psi, \iota, \varphi_o\}$. To derive a unique location for each source we use a cylindrically symmetric disk model of the galaxy with an exponential falloff in both the radial and vertical directions,

$$\rho = \rho_o e^{-r/r_o} e^{-|z|/z_o}. \quad (5)$$

Here ρ_o is the space density at the galactic center, r_o is the radial scale length, and z_o is the vertical scale height of the galactic disk. The values of r_o and z_o vary with the different types of binaries (i.e. cataclysmic variables, white dwarf binaries, etc.), but all types are assumed to obey the above model. The binary positions are simply de-

scribed in galactocentric-cylindrical coordinates. The natural coordinate system for the LISA mission is heliocentric-ecliptic coordinates. Therefore, once the positions for the binaries are selected using the galactic position distributions, they are translated to the LISA coordinate system through a series of standard coordinate transformations.

The observed orientation of a binary system is set by the principal polarization angle ψ and the inclination angle ι . The inclination angle is defined as the angle between the line of sight to the binary \hat{n} and the angular momentum vector of the binary \vec{L} . The inner product of \hat{n} and the angular momentum directions $\hat{n} \cdot \hat{L}$ is taken to be uniformly distributed between -1 and 1 . The principle polarization angle describes the orientation of the semimajor axis of the projected binary orbit on the celestial sphere and is uniformly distributed between 0 and π . The distribution for φ_o , which describes the positions of the binary components at time $t = 0$, is uniformly distributed between 0 and 2π .

B. Intrinsic parameters

The distributions for each intrinsic parameter $\{M_1, M_2, P_o\}$ depends on the binary type under consideration. To model each of these parameters, we used the distributions given in HBW. For this reason our galactic backgrounds include W UMa (3×10^7), cataclysmic variables (1.8×10^6), neutron star–neutron star (10^6), black hole–neutron star (5.5×10^5), and close white dwarf (3×10^6) binaries. The quantities in the parentheses indicates how many systems of that type are included in the simulation. Note that for most of our analyses we use the 10% reduced population of close white dwarf binaries as described in HBW as this allows us to compare directly with prior results.

We have elected not to include the unevolved binaries. The reason for this is that they are predominately very low frequency sources ($\lesssim 10^{-5}$ Hz). As a result, their signals will be buried in the instrumental noise and, therefore, will not contribute to the observed galactic background.

C. Barycentric background

Many of the prior studies of the galactic background approached the problem by estimating the net gravitational wave luminosity as a function of frequency in the Solar System barycenter. From the luminosity they then derive a gravitational wave strain amplitude using [14]

$$h = \left(\frac{16\pi G}{c^3 \omega_{gw}^2} \frac{L_{gw}}{4\pi r^2} \right)^{1/2}, \quad (6)$$

where ω_{gw} and L_{gw} are the gravitational wave angular frequency and luminosity, respectively.

In order to make comparisons between our results and prior studies, we must relate the above expression for the strain amplitude to quantities calculated in our

Monte Carlo simulation. To this end, we first note the relationship between gravitational wave luminosity and flux [15],

$$\frac{L_{gw}}{4\pi r^2} = F_{gw} = \frac{c^3}{16\pi G} \langle \dot{h}_+^2 + \dot{h}_\times^2 \rangle, \quad (7)$$

where the angle brackets denote an average over several gravitational wave periods. Using this relationship the strain amplitude is rewritten as

$$h = \left(\frac{1}{\omega_{gw}^2} \langle \dot{h}_+^2 + \dot{h}_\times^2 \rangle \right)^{1/2}. \quad (8)$$

From the waveforms given in Eq. (2) it follows that

$$h = \left(\frac{1}{2} (A_+^2 + A_\times^2) \right)^{1/2}. \quad (9)$$

The polarization amplitudes, A_+ and A_\times , are functions of the binary masses, distance to the source, orbital period, and inclination angle [see Eq. (3)].

Equation (9) gives the strain amplitude for a single source. To mimic a power spectrum in the Solar System barycenter frame, we first bin the sources according to their frequencies. The bin widths are $\Delta f = 1/T$, where T is the total observation time (for our simulations T is set to one year). Once the sources are sorted the net strain amplitude per frequency bin is calculated from

$$h_{\text{net}} = \left(\frac{1}{2} \sum_{i=1}^{N_b} (A_+^2 + A_\times^2)_i \right)^{1/2}, \quad (10)$$

where N_b is the number of sources in the bin. Note that Eq. (10) accounts for constructive and destructive interference in the same way as in standard data analysis uncorrelated, random errors add quadratically with the square root taken after all errors have been included. Similarly for the background, the net strain amplitude is the square root of all individual polarization amplitudes added quadratically.

Figure 1 compares our Monte Carlo results to HBW. (Note that the plots show spectral amplitudes h_f , not strain amplitudes h . For monochromatic binaries the two are related by $h_f = \sqrt{T}h$ where T is the observational period.) The HBW galaxy model includes W Ursae Majoris (W UMa) contact binaries, Cataclysmic Binaries (CB), Neutron Star–Neutron Star (NS-NS) binaries, Black Hole–Neutron Star (BH-NS) binaries, and White Dwarf–White Dwarf (WD-WD) binaries. For each binary class we are in agreement. The smearing effect seen at high frequencies is due to empty bins in the spectrum. For the compact binaries the orbital period distributions have a small, but finite, probability at short periods. Consequently, it takes a large number of draws against the period distribution to produce a source with an extremely short period. In the cases of the neutron star–neutron star and close white dwarf binaries, the probability in the period distribution tails becomes small enough that for the number of sources included in our simulated background one would not expect a large number of extremely short period

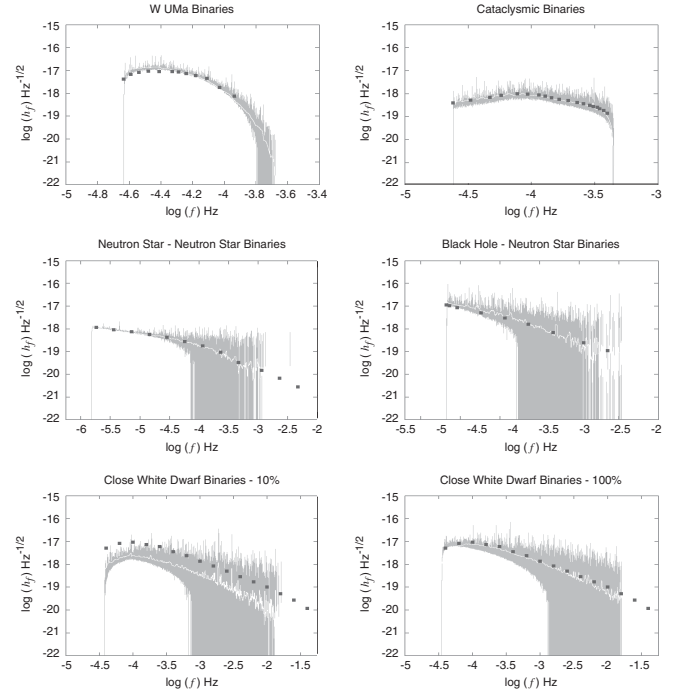


FIG. 1. A comparison of our full Monte Carlo simulation (gray) and a running average of the simulation (white) to those of HBW (squares). For each binary type we are in agreement. To ease comparison, the final figure shows a background using the full realization of white dwarf binaries. However, our simulated background uses the 10% reduced white dwarf population.

(high frequency) sources. This is why the HBW data extends beyond our simulated backgrounds.

Figure 2 shows the total galactic background as viewed in the barycenter frame. The sharp rise in the background at

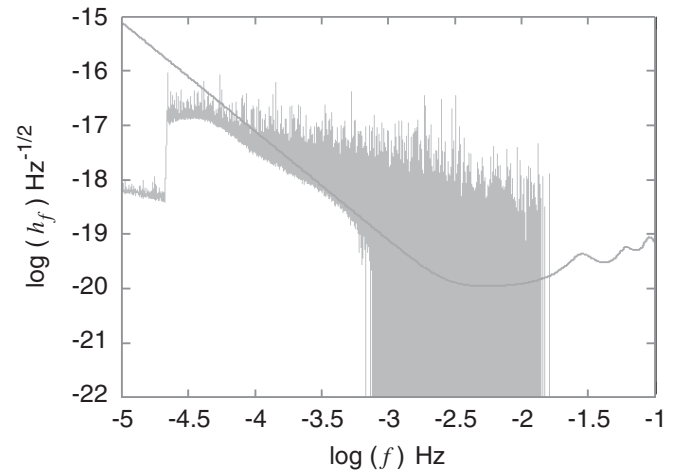


FIG. 2. A realization of the galactic background as observed in the barycenter frame. The dark line is the all-sky and polarization averaged LISA sensitivity curve [25]. The jump at $10^{-4.6}$ Hz is due to sudden increase in the number of W UMa binaries. Had we included a realization of the unevolved binaries, the background levels would be roughly constant below $10^{-4.6}$ Hz with a spectral amplitude of $h_f \approx 10^{-17} \text{ Hz}^{-1/2}$.

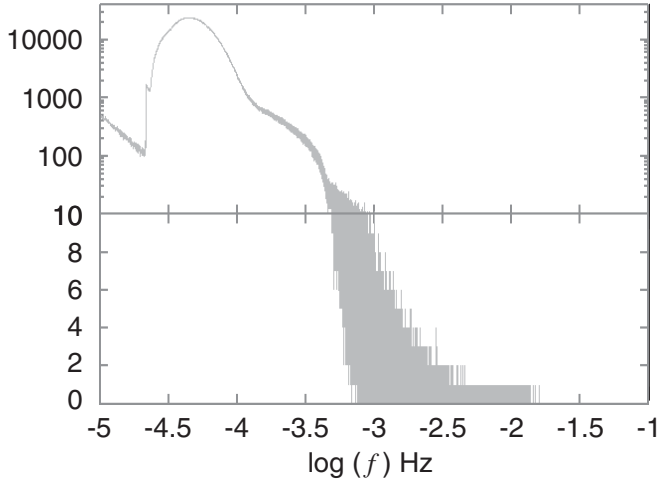


FIG. 3. Number of sources per frequency bin. Again the dip in the number of sources at $10^{-4.6}$ Hz is associated with the neglected unevolved binaries.

$f = 10^{-4.6}$ Hz is due to the sudden increase in the number of W UMa binaries. The signal below $f = 10^{-4.6}$ Hz is due to neutron star–neutron star binaries. If the unevolved binaries had been included, the galactic background would be approximately constant between 1 and 100 μ Hz at a level of $h_f \approx 10^{-17} \text{ Hz}^{-1/2}$.

As Nelemans *et al.* [6] found with their population synthesis models of the galaxy, when the individual sources are modeled the background appears spiky. The large fluctuations in the background are due to a small number of bright sources. As we will show later, when these sources are removed from the background the spectrum becomes smooth.

It is generally agreed that a confusion limited background arises when the average number of source per frequency bin is larger than unity. (Additionally the net strain per bin must also be larger than the intrinsic detector noise.) Figure 3 shows that the peak number of sources per bin is in excess of 10^5 near 0.04 mHz. The plot also demonstrates that for a large portion of LISA’s spectrum the number of sources per bin is greater than ten.

III. DETECTOR BACKGROUND

The backgrounds presented in the previous section were not convolved with a model for the instrument response. As with all fields of astronomy, the act of measuring incident radiation has to be properly understood in order to correctly interpret the signals. In this section we first summarize the LISA mission and then describe our models for the detector response. We then present the simulated galactic background as measured by the detector.

LISA is a joint ESA/NASA mission planned for launch around 2015. The mission consists of three identical spacecraft in separate, slightly eccentric, heliocentric orbits inclined with respect to the ecliptic plane [16]. The orbits are

carefully chosen such that the spacecraft constellation will form, and approximately maintain, an equilateral triangle with a mean spacecraft separation of 5×10^6 km. The center of the constellation, referred to as the guiding center, will have an orbital radius of 1 AU and trail the Earth by 20° . During the course of one orbit, the constellation will cartwheel once with a retrograde motion as seen by an observer at the Sun. LISA is sensitive to gravitational radiation in the range of 10^{-5} to 1 Hz.

The detector’s motion introduces amplitude (AM), frequency (FM), and phase modulations (PM) into the gravitational wave signals [9]. The amplitude modulation originates from the detector’s motion sweeping the antenna pattern across the sky. The phase modulation results from the differing responses to each polarization state. The frequency (Doppler) modulation is due to the motion of the detector relative to the source. Since the bulk orbital and cartwheel motions both have a period of one year, the resulting modulations appear as sidebands in the power spectrum separated from the instantaneous carrier frequency by integer values of the modulation frequency, $f_m = 1/\text{year}$.

For our studies the detector response is modeled using a combination of the *Extended Low Frequency Approximation*, which is developed in the appendix, and the *Rigid Adiabatic Approximation* as described in Ref. [17]. As explained in the appendix, to save on computational costs it is advantageous to simulate the detector response directly in the frequency domain where a quasimonochromatic source will only have a small number of sidebands. At low frequencies, the bandwidth for a slowly evolving circular binary is

$$B = 2 \left(4 + \frac{2\pi f R}{c} \sin(\theta) \right) f_m, \quad (11)$$

where $R = 1$ AU is the orbital radius of LISA and θ is the colatitude of the source on the celestial sphere. For sources with gravitational wave frequencies below a few millihertz, the bandwidth is less than $100f_m$ and we can achieve a considerable saving in computational cost by working in the frequency domain. At higher frequencies the sources have larger bandwidths, more complex modulation patterns, and signals that evolve significantly in frequency, making them harder to model directly in the frequency domain.

In the appendix it is shown that the *Extended Low Frequency Approximation*, which is applied in the frequency domain, is only valid for frequencies below 7 mHz. For the few hundred signals with a carrier frequency above this cutoff, we use the more accurate time domain response model, the *Rigid Adiabatic Approximation*. To combine the results from each approximation, we first simulate the response for the signals that are above 7 mHz using the more detailed *Rigid Adiabatic Approximation* and add them linearly in the time domain. We then perform a fast Fourier transform. For the sources that are

simulated directly in the frequency domain, we coherently add the signals by summing the real and imaginary parts of their respective Fourier coefficients at each frequency. By adding the coefficients we maintain the phase information which dictates the constructive and destructive interference of the gravitational waves. The final detector response is the sum of the Fourier coefficients from the extended low frequency and adiabatic results. It is also at this time that we add in a detector noise realization using the prescription given in Ref. [17]. Figure 4 shows a particular realization for a Michelson signal in the frequency domain. Figure 5 shows the same signal in the time domain.

In comparing the background as observed in the detector frame (Fig. 4) versus in the barycentric frame (Fig. 2), a striking feature is that it is lower by roughly a full decade across the entire spectrum. The reduction is due to two effects. The first effect is the detector efficiency, which relates the total signal power in the detector to the total signal power at the barycenter. The all-sky and polarization averaged detector efficiency is equal to $\sqrt{3/20}$ at low frequencies, and gets progressively worse at high frequencies. (This is immediately evident by comparing the sensitivity curve in Fig. 2 to the average Michelson noise in Fig. 4.) The second effect is due to the orbital motion of the detector. In the barycentric frame, most galactic binaries are well approximated as monochromatic. As LISA moves in its orbit the monochromatic signals are modulated across multiple frequency bins. At high frequencies the spreading effects are evident by spectral power showing up in bins that were previously empty in the barycenter frame. At low frequencies the expectation is that the spreading from adjacent bins will cancel out due to the numerous sources found in each bin (see Fig. 3). However, as will be shown in the next two sections, the galactic background is

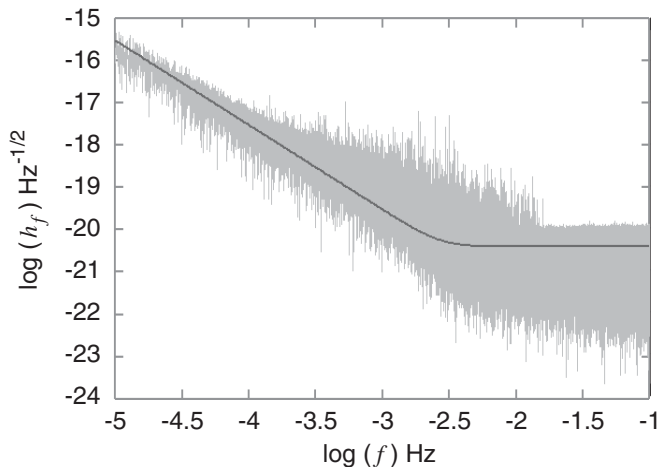


FIG. 4. A realization of the HBW 10% galactic background as measured in the detector's frame. The dark line is the average Michelson noise associated with the detector. The galactic gravitational wave background is evident in the spiky structure between 0.1 and 10 mHz.

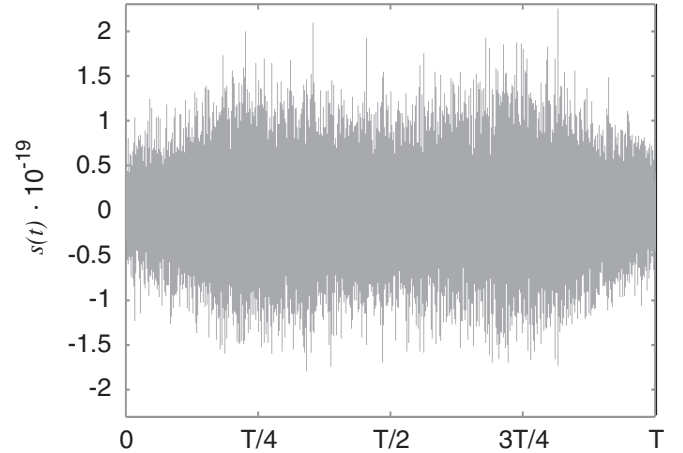


FIG. 5. A realization of the HBW 10% galactic background as measured in the detector's frame shown in the time domain (with no instrument noise). The annual modulation of the signal due to the detector motion is apparent by the two large lobes.

dominated by a few bright sources. When the bright sources are modulated there is not a compensating bright source in the adjacent bin. As a result, the galactic background is also reduced at lower frequencies.

IV. STATISTICAL CHARACTER OF THE GALACTIC BACKGROUND

Of great interest to the LISA mission is to broadly characterize the galactic gravitational background in a statistical sense. Such a characterization is essential to the development and implementation of data analysis algorithms which often make assumptions about the character of the noise.

In the spectral regions of LISA's band where the galactic background dominates the detector response, the background becomes a source of noise. By inspection of the spectrum in Fig. 4, the galaxy is evident by the jaggedness between 0.1 and 10 mHz. Outside this region the galactic binary signals are weaker than the intrinsic detector noise. This is evident in the plot by the relative smoothness of the spectrum from bin-to-bin. One way to characterize the background is to statistically study the Fourier coefficient distributions in different regions of the spectrum. Of specific interest is finding out if the galactic background is characterized by a Gaussian distribution.

Tests for Gaussianity are done using independent χ^2 and Kolmogorov-Smirnov tests. The Gauss tests are performed over a window of 512 bins and done at each frequency. Figure 6 shows the results of the Kolmogorov-Smirnov test performed on the real coefficients for the spectrum shown in Fig. 4. The p values plotted along the ordinate axis are the probabilities that the set of measured deviates are Gaussian distributed. While it is impossible to say with certainty that a set of measured deviates are necessarily distributed with a specific distribution, they can be shown

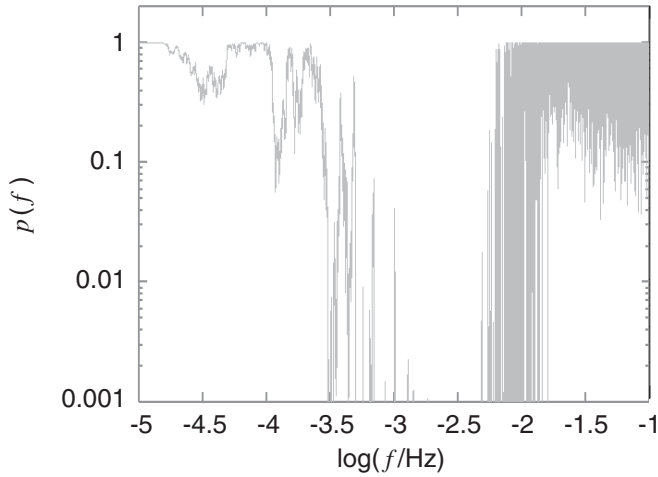


FIG. 6. The Kolmogorov-Smirnov Gaussianity test applied to the real Fourier coefficients for the detector output shown in Fig. 4. The presence of the galactic background is apparent by the low p values about $f = 10^{-3}$ Hz. Similar results are found for the imaginary coefficients, for the other data channels, and when using a χ^2 test.

not to agree. Values for p above a hundredth are usually accepted as agreeing with the tested distribution function. Values of p below a hundredth, which are seen in the millihertz region, indicate that the measured data are not Gaussian distributed.

Comparing the results of the Gaussian test (Fig. 6) and the original LISA output (Fig. 4) indicates that the detector response is non-Gaussian for frequencies in which the background is above the intrinsic detector noise level. Outside these regions, where the detector's noise dominates the output, the returned p values are consistent with a Gaussian distribution, as they should since the simulation of the noise is based on Gaussian distributions. Similar results are found for the imaginary coefficients, other channels of data, and when calculated using a χ^2 test.

A common misconception is that the galactic background should be Gaussian distributed. This assumption is based on the Central Limit Theorem, which states that for a large sample of random deviates, regardless of their parent distribution, the distribution of average values will be approximately Gaussian. However, the Central Limit Theorem is not directly applicable to the galactic background since the net power in a single frequency bin may be dictated by a single bright source.

V. CONFUSION LIMITED BACKGROUND

A. Gaussian nature of the confusion limited background

Large fluctuations originating from bright sources cause the tails of the expected Gaussian distributions to be enlarged. If the bright sources were removed from the data streams, then the remaining background would be

Gaussian. To demonstrate this we first identify the bright sources, subtract them, and then retest the remaining background for Gaussianity.

Identifying all the bright sources in the actual LISA data streams is a difficult problem not yet fully solved. The modulation effects caused by LISA's orbital motion spread a source's spectral power across multiple frequency bins. Although the bandwidth over which a signal will spread is a known function of the gravitational wave frequency and sky position, if multiple signals are overlapping in a small region of frequency space, the true number of signals in the region may not be clearly identifiable. For our Monte Carlo models, when we generate each binary, the parameter values for each system are known. With this extra information we can quickly and accurately identify bright sources and remove them from the data streams.

Our approach to identifying bright sources is to categorize them according to their signal-to-noise (SNR) ratio using the standard formula,

$$(\text{SNR})^2 = 4 \int_0^\infty \frac{|\tilde{h}(f)|^2}{S_n(f)} df, \quad (12)$$

where $\tilde{h}(f)$ is the Fourier transform of the noiseless response to a single gravitational wave signal, and $S_n(f)$ is the one-sided noise power spectral density. A source is labeled as "bright" if its SNR is greater than 5 (optimistic) or 10 (conservative). The proper use of Eq. (12) requires a clear interpretation of the noise. We are interested in removing sources that are bright relative to the local power spectrum level. Therefore, the $S_n(f)$ curve must be a composite of the intrinsic detector noise and the galactic background. It is an effective noise for the detector, which we will emphasize by denoting it as $S_n^{\text{eff}}(f)$.

To approximate the effective noise we calculate the median detector output. While representing the effective noise by the median response (as opposed to the mean response) is somewhat stable against bright sources, in regions near an extremely large SNR signal or where the density of bright sources is large, the median will still be influenced by these few signals. To account for the influence of the bright sources in calculating the $S_n^{\text{eff}}(f)$ curve, we perform our calculations iteratively. We start with the median response of the initial output and calculate the number of bright sources with reference to this curve. We then remove the bright sources exactly using the same detector response approximation that generated them. The justification for using the exact parameters is a matter of simplicity, since data analysis algorithms are still being developed. Moreover, with a SNR threshold of 10 the errors in the recovered parameters will be small. The result of removing the bright sources is a new background from which we can calculate a new median response. From the new median response we calculate the number of bright sources with respect to the new $S_n^{\text{eff}}(f)$ curve. We iterate this procedure until there are no new bright sources being

identified. In some examples, such as with the 100% HBW model, the procedure does not appear to converge, so the subtraction was stopped after 10 iterations.

Previous estimates [4,11] of the confusion background ignored the relative brightness of the sources and focused instead on the source density. These estimates defined the confusion regime in terms of the number of sources per frequency bin. Outside of the confusion regime sources could be resolved and removed, while inside the confusion regime the sources acted as a source of noise. This notion of source confusion is based on linear algebra: The signal from each galactic binary is described by 7 or 8 parameters [18], and there are 4 data points per frequency bin (two independent channels, each with a real and imaginary part). Thus, one needs at least 2 frequency bins per source to have as many data points as there are unknowns. While this estimate is very crude, it is unlikely that a data analysis algorithm can be found that beats the 0.5 source per bin saturation point by very much (methods such as maximum entropy [19] introduce priors that can help tame under constrained systems, but they can only do so much). In order to study the effect of a source density cutoff, we repeat the SNR based source subtraction procedure with a maximum resolved source density of 0.25 sources per bin using a 100 bin average. The density of one source per four bins was chosen as intermediate between the capabilities of existing algorithms [20] and the saturation point described above.

Table I lists the number of bright sources removed at each iteration and the total number of bright sources removed for several different realizations of the galactic background if no source density cutoff is applied. In each of the three HBW 10% realizations, the total number of sources was fixed at 3.635×10^7 . All three realizations gave similar results. The results of a HBW background using the full 100% of the white dwarves, along with the NYZ white dwarf background (2.6×10^7 sources) are also

TABLE I. Number of new bright sources identified at each iteration.

Iteration	10%					
	10%(1)	10%(2)	10%(3)	100%	(SNR = 5)	NYZ
1	6795	6848	6793	10736	14346	8583
2	3806	3723	3712	8084	10620	4803
3	1693	1803	1846	5340	5480	2090
4	817	929	866	3550	2577	866
5	395	457	456	2597	1129	473
6	226	250	225	2014	525	266
7	114	172	123	1628	278	191
8	59	97	76	1400	144	125
9	1264	72	...
10	1136	38	...
Total	13905	14279	14097	37749	35209	17396

TABLE II. Number of new bright sources identified at each iteration with a source density cutoff applied.

Iteration	10%	100%	10% (SNR = 5)	NYZ
1	6795	10736	14346	8583
2	3751	7850	4898	4803
3	1669	4440	194	2007
4	724	1531	20	732
5	271	463	1	325
6	79	157	...	186
7	30	66	...	79
8	12	1	...	48
9	7	27
Total	13338	25244	19459	16788

shown. For comparison we also include the optimistic case of using a subtraction threshold of SNR = 5.

Table II lists the number of bright sources removed at each iteration and the total number of bright sources removed for several different realizations of the galactic background when a maximum density of 0.25 resolved sources per bin is applied. The HBW 10% and NYZ models are only slightly affected by the cutoff, while the HBW 100% and SNR > 5 version of the HBW 10% model are significantly affected. The impact of the cutoff is evident in Fig. 7, where the effective noise levels for the HBW 100% (SNR > 10) and HBW 10% (SNR > 5) models are shown with and without the source density cutoff applied.

Shown in Fig. 8 is the same Michelson signal as before (Fig. 4), but with the bright sources removed. Visual inspection of the spectrum shows that without the bright sources the bin-to-bin fluctuations are much smaller; an indication that the Fourier coefficients may be Gaussian

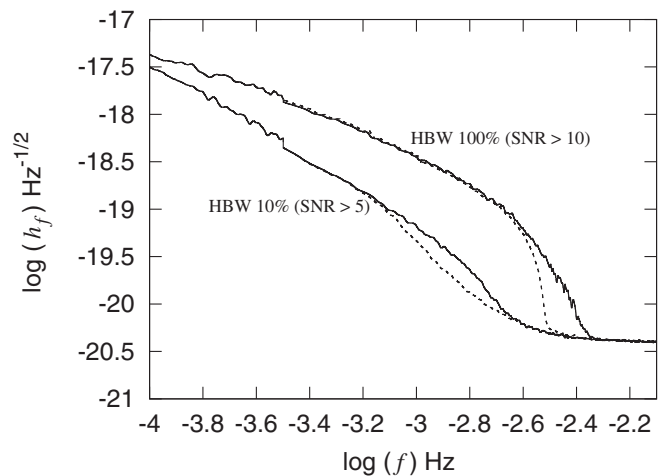


FIG. 7. Effective noise levels for the HBW 100% (SNR > 10) and HBW 10% (SNR > 5) models with (solid) and without (dotted) a source density cutoff of one resolved source per four frequency bins.

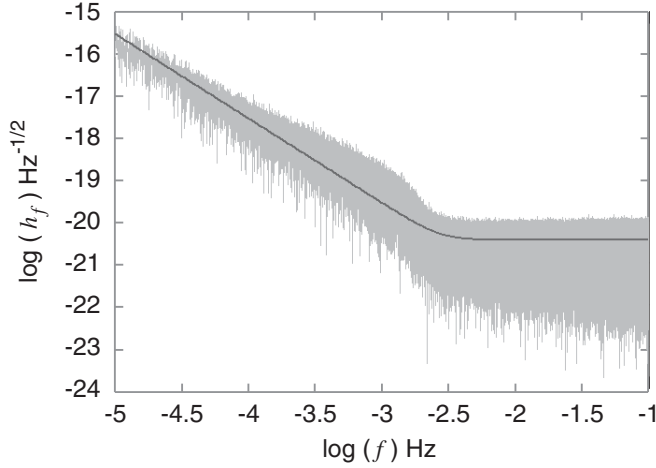


FIG. 8. The same Michelson signal from before, but after the $\sim 10^4$ bright sources have been removed from the data streams.

distributed. Figure 9 confirms this hypothesis. When the bright sources are removed from the data streams the galactic background is Gaussian in nature.

B. Confusion limited background estimate

The sources that are not flagged as bright will give rise to a confusion limited background that acts as an effective noise source for LISA. Taking the list of unresolved sources that remain after the simulated data analysis procedure described in the previous section, we can generate estimates of the confusion noise in either the barycentric frame or in the instrument data channels. The former is useful for making comparisons with earlier work, while the latter is better suited to studying the effect of the confusion background on LISA's ability to resolve other types of gravitational wave signals.

Figure 10 compares our barycenter and detector frame confusion noise estimates to the barycenter estimate of

$$S_{\text{conf}}(f) = \begin{cases} 10^{-45.9} f^{-2.6} & 10^{-4.4} < f \leq 10^{-3.2} \\ 10^{-50.38} f^{-4.0} & 10^{-3.2} < f \leq 10^{-2.8} \\ 10^{-78.38} f^{-14.0} & 10^{-2.8} < f \leq 10^{-2.65} \\ 10^{-126.08} f^{-32.0} & 10^{-2.65} < f \leq 10^{-2.55} \\ 10^{-62.33} f^{-7.0} & 10^{-2.55} < f \leq 10^{-2.1} \end{cases} \text{ m}^2 \text{ Hz}^{-1}. \quad (13)$$

Similarly, for the NYZ white dwarf binary background we found

$$S_{\text{conf}}(f) = \begin{cases} 10^{-44.62} f^{-2.3} & 10^{-4.0} < f \leq 10^{-3.0} \\ 10^{-50.92} f^{-4.4} & 10^{-3.0} < f \leq 10^{-2.7} \\ 10^{-62.8} f^{-8.8} & 10^{-2.7} < f \leq 10^{-2.4} \\ 10^{-89.68} f^{-20.0} & 10^{-2.4} < f \leq 10^{-2.0} \end{cases} \text{ m}^2 \text{ Hz}^{-1}. \quad (14)$$

These fits do not include instrument noise, and have been quoted in terms of position noise in order to avoid ambiguities in the path length scaling. (Our simulations nor-

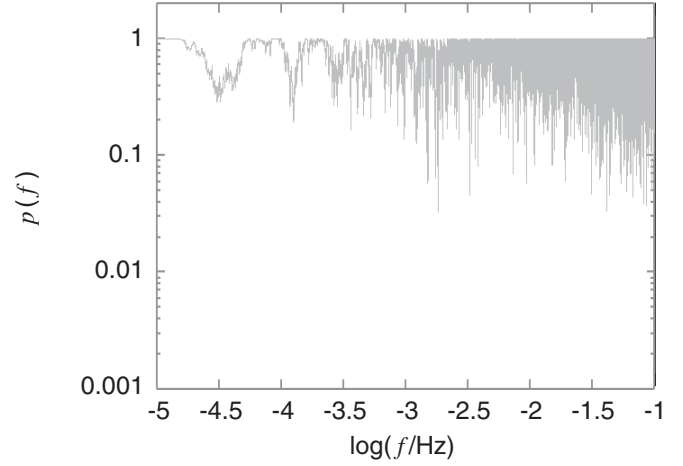


FIG. 9. A running Gauss test applied to the detector output after the bright sources have been removed. Unlike before, all returned p values are consistent with a Gaussian distribution.

Ref. [4]. We have multiplied our detector frame result by a factor of $\sqrt{20/3}$ to account for the average detector efficiency. Our estimate is lower than the estimate in Ref. [4] at low frequencies and higher at high frequencies. It is important to note that both estimates use exactly the same HBW model for the compact galactic binaries. The differences in the confusion noise estimates are due to the different way in which we modeled the data analysis procedure. Note that our results can only be compared below ~ 1.3 mHz. Above this frequency the Ref. [4] estimate is dominated by extragalactic sources, which we did not include in our simulation.

A simple piecewise fit to our confusion noise estimate of the HBW 10% background in the detector frame is given by

malize by the round-trip path length, while other studies normalize by the detector arm length.) For comparison, our simulations of the Michelson response used an instrument

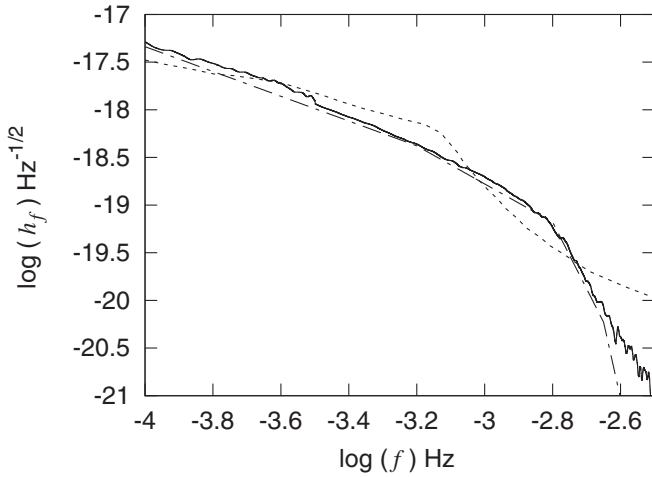


FIG. 10. Our estimates for the HBW 10% barycenter (solid line) and detector frame (dot-dashed line) confusion noise levels compared to the Ref. [4] estimate (dotted line). Our detector frame confusion noise has been multiplied by a factor of $\sqrt{20/3}$ to account for the average detector efficiency.

noise spectral density

$$S_n(f) = \frac{1}{4L^2} \left[4S_{\text{pos}} + 8(1 + \cos^2(f/f_*)) \frac{S_{\text{accl}}}{(2\pi f)^4} \right] \quad (15)$$

with position noise $S_{\text{pos}} = 4 \times 10^{-22} \text{ m}^2 \text{ Hz}^{-1}$ and acceleration noise $S_{\text{accl}} = 9 \times 10^{-30} \text{ m}^2 \text{ s}^{-4} \text{ Hz}^{-1}$. The choice of instrument noise level only has a weak effect on our results as the unresolved galactic background is the main source of noise from 0.1 mHz to roughly 3 mHz.

A true confusion limited background is what remains after a full data analysis procedure has removed all identifiable signals. At present such an algorithm has not been fully implemented, though good candidates now exist [20,21]. Our method of removal, by which we remove a source using the same response approximation that included it, mimics a true data analysis procedure, but it fails to include some of the subtle nuances associated with signal and noise confusion [21]. Though we did not use a true source removal algorithm, we expect that Fig. 8 represents a good approximation to how the confusion limited background will appear in the LISA output. The best estimates of the confusion noise may ultimately come from Bayesian methods which treat the effective noise level as another model parameter to be estimated [22].

Figure 11 shows the effective noise levels (confusion + instrument noise) for the HBW 10% and the NYZ models. These estimates were produced using the conservative $\text{SNR} = 10$ criteria for bright source subtraction, and a maximum density of 0.25 resolved sources per bin. In contrast to what we found with the HBW 100% and HBW 10% ($\text{SNR} \geq 5$) models, the effective noise levels are little changed by the source density cutoff. Also shown is the effective noise estimate used by Barack and Cutler [11]. The Barack-Cutler curve agrees quite well with our

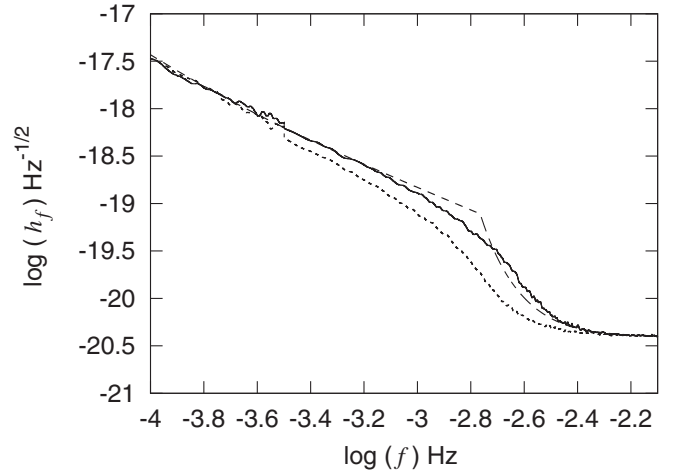


FIG. 11. Estimates of the effective noise level for the HBW 10% model (dotted line), and the NYZ model (solid line). The effective noise curve used by Barack-Cutler Curve (dashed line) is also shown.

NYZ curve, though it does slightly overestimate the noise level between 0.5 and 2 mHz.

VI. BRIGHT SOURCE STATISTICS

The bright sources represent signals that are identifiable in LISA's output. By understanding their location and separation (in the frequency domain) proper data analysis tools can be developed and applied in the search for their signals in the detector output. Also of interest are the

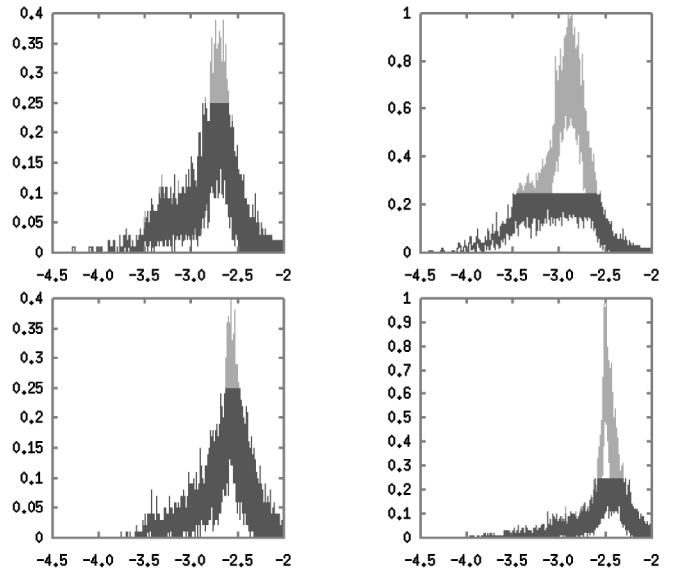


FIG. 12. The accumulated number of bright sources per frequency bin using a 100 bin average, both with (black) and without (gray) a bright source density cutoff. Starting in the upper left and going clockwise we have: HBW 10% with $\text{SNR} \geq 10$, HBW 10% with $\text{SNR} \geq 5$, HBW 100% with $\text{SNR} \geq 10$, and NYZ with $\text{SNR} \geq 10$.

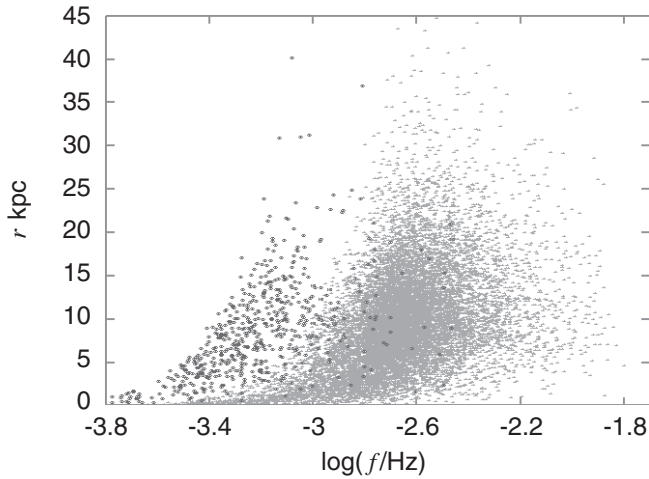


FIG. 13. Distribution of outlier distances as a function of their frequency. Filled squares are white dwarf binaries, open circles are black hole–neutron star binaries, asterisks are neutron star binaries, and open squares are cataclysmic binaries.

properties of the bright sources. Are they near to us or distributed throughout the galaxy? Can we identify the type of binary system? The next two sections address these issues.

A. Bright source density

For issues concerning data analysis, an interesting quantity to know is the number of bright sources per frequency bin. Figure 12 is a plot of the average number of bright sources per frequency bin using a 100 bin window to calculate the average. The peak densities occur at ~ 2 mHz for the HBW 10% and NYZ models, whereas the HBW 100% model has a maximum at ~ 3 mHz. For the HBW 100% (SNR ≥ 10) model and the HBW 10% (SNR ≥ 5) model the maximum bright source density reached one source per bin. This is why the resolved source density cutoff of 0.25 made such a big difference in those cases. The bandwidth of a typical source at this frequency is approximately 20 frequency bins (for one year of observation). As a result, in the peak density region there are bright sources whose power at least partially overlaps.

B. Bright source characteristics

An interesting question to ask is what property makes a particular binary bright. At high frequencies, where the number of sources per bin is less than unity, a source is considered bright if its signal is greater than the intrinsic detector noise. However, at low frequencies, where the number of sources per bin can be in the thousands (see Fig. 3), each source must compete against the other sources in the bin to become detectable.

To see what makes a source bright at low frequencies, recall the functional form of the intrinsic amplitude,

$$\mathcal{A} = \frac{2G^2 M_1 M_2}{c^4 r} \left(\frac{4\pi^2 f_{orb}^2}{G(M_1 + M_2)} \right)^{1/3}. \quad (16)$$

Given a particular frequency bin the orbital frequency does not vary by more than a bin width, leaving only the masses and the distance to the source to determine if a signal is bright.

Figure 13 shows the distance versus frequency for each bright binary coded by the type of system it is. Evident from this figure is the mass segregation associated with the bright systems. At low frequencies, where the number of sources per bin peaks, the more massive black hole–neutron stars are detectable. At higher frequencies the black hole neutron star binaries are less numerous (see Fig. 1) and the white dwarf binaries dominate the list of bright sources.

To associate a binary to a particular type requires estimating the component masses. Unfortunately for sources whose frequency evolution is too small to detect, there is a mass-distance degeneracy that prevents direct mass measurements [23]. Table III shows the number of the bright sources that evolve by a measurable amount. The frequency evolution is considered measurable if the change in gravitational wave frequency during the time of observation T_{obs} is greater than the width of a frequency bin ($1/T_{obs}$).

It is interesting to note that very few sources will have a measurable frequency evolution during one year of observation. The two main reasons for this is that the frequency evolution is dictated by mass and initial frequency [see Eq. (4)]. The massive black hole–neutron star binaries are

TABLE III. Number of subtracted binaries by type.

Type	Included	Realization 1		Realization 2		Realization 3	
		Removed	Evolving	Removed	Evolving	Removed	Evolving
W UMa	3×10^7	0	0	0	0	0	0
CB	1.8×10^6	1	0	2	0	1	0
NS-NS	10^6	11	0	11	2	7	0
BH-NS	5.5×10^5	591	10	585	12	550	8
WD-WD	3×10^6	13 302	346	13 681	353	13 539	337
Total	3.635×10^7	13 905	356	14 279	367	14 097	345

located at low frequencies, while the higher frequency white dwarf binaries have smaller chirp masses.

Figure 13 also demonstrates that we should be able to see individual binaries distributed throughout the galaxy. This introduces the tantalizing prospect of using gravitational wave data to map galactic populations. However, since there is a mass-distance degeneracy for systems that do not evolve appreciably during the lifetime of the detector, only a small fraction of the identifiable sources can be used for such an analysis.

VII. SUMMARY AND CONCLUSIONS

In this paper we have presented a Monte Carlo simulation of the galactic gravitational wave background as it would be detected by the proposed LISA mission after one year of operation. For the intrinsic binary properties we used the distributions given in Hills *et al.* [3] and Nelemans *et al.* [8]. Our key findings are: the galactic background levels will be reduced in the detector frame as compared to the barycenter frame, prior to the removal of the bright sources the background is not characterized by a Gaussian distribution, and of the $\sim 10^4$ identifiable sources only $\sim 10^2$ are evolving and thus identifiable by type. We have also derived a new estimate for the confusion limited background that differs from other estimates given in the literature. Below 1 mHz our estimate is lower than previous estimates, while above 1 mHz our estimate is higher than previous findings. Our calculation of the bright source density (in frequency space) suggests that data analysis algorithms can be developed that are capable of resolving $\sim 10\,000$ galactic binaries from a one year LISA data stream. Of these, roughly 300 will be measurably chirping, allowing the determination of the chirp mass and the distance to these sources. The number of resolvable galactic sources, especially the number of measurably evolving systems, will increase significantly after several years of observation (the resolution of the frequency derivative improves with observation time, T_{obs} , as $T_{\text{obs}}^{5/2}$).

An important point to keep in mind about the results presented here is that they assumed particular descriptions for the galactic distribution, total number, and source characteristics of each binary population. A different collection of models of the extrinsic parameters may return a slightly different set of results as is seen in the NYZ backgrounds. However, the main conclusions drawn here are largely dictated by three quantities, the total number of binary systems, their period distributions, and the component masses.

The number of binary sources in the galaxy can impart a noticeable difference in the background levels. As radiation from the binaries converges on the detector, the random phase differences will cause constructive and destructive interference. Statistically the problem is analogous to a random walk. As a result, the net spectral amplitude per frequency bin will grow as \sqrt{N} . For every

factor of 100 difference in the number of sources, the background levels raise or lower by a decade, respectively. For electromagnetically visible binaries (W UMa, unevolved, and cataclysmic binaries), galactic surveys have placed stringent constraints on the total number of such binaries. However, for the compact binaries (neutron star–neutron star, black hole–neutron star, and white dwarf binaries) equivalent surveys have failed to place strict bounds on the total numbers. One return of the LISA mission will be to place limits on the populations by measuring the galactic background median levels and the number of bright sources from each population.

While the overall level for the galactic background level is partially influenced by the total number of systems, the background level is also dictated by the component masses via Eq. (16). By comparing our HBW based simulations to the population synthesis approach of NYZ [8], we have found that relatively small changes in the component masses can lead to significant changes in the background levels. Current uncertainties in the true mass distributions arise from a lack of observational data and a theoretical understanding of mass transferring stages during formation. The NYZ white dwarf binaries are typically composed of two light components, $M < 0.5M_{\odot}$, whereas the HBW white dwarf binaries are typically composed of one light component and one heavy component, $M > M_{\odot}$. This results in the HBW systems having mean chirp masses, $\mathcal{M} = (M_1 M_2)^{3/5} / (M_1 + M_2)^{1/5}$, almost a factor of 2 higher than the NYZ systems. Since the amplitude of signals scales as $\mathcal{M}^{5/3}$, the difference in component masses translates into a factor of ~ 3.2 increase in the HBW background relative to the NYZ background for the same source density. It is an interesting numerical coincidence that the 10% reduction in source density proposed by HBW yields a $\sqrt{10} \sim 3.2$ reduction in the amplitude of the background, resulting in a background level comparable to the NYZ model. Despite this fortuitous cancellation, the HBW 10% and the NYZ models yield different confusion noise estimates due to the reduced number of sources in the HBW 10% model.

The period distributions will also impart a noticeable change in the background. If, for example, there is a mechanism that suppresses low period white dwarfs, the values in Table III and Fig. 13 would change. Conversely, we can invert the problem and ask questions such as what would the high frequency end of the galactic background look like if certain physics are included in the models for close white dwarf binary production?

ACKNOWLEDGMENTS

We are very grateful to Gils Nelemans for providing us with a realization of his white dwarf background. We would like to thank Peter Bender for helpful discussions concerning the confusion limited background. This work was supported by the NASA EPSCoR program through

Cooperative Agreement No. NCC5-579. L. J. R. and S. E. T. acknowledge the support of the Center for Gravitational Wave Physics. The Center for Gravitational Wave Physics is supported by the NSF under Cooperative Agreement No. PHY 01-14375.

APPENDIX: DETECTOR RESPONSE

For a gravitational wave traveling in the \hat{k} direction we can express a single channel LISA response as a linear sum of responses for each polarization state,

$$s(t) = A_+ F^+(t) \cos\Phi(t) + A_\times F^\times(t) \sin\Phi(t), \quad (\text{A1})$$

where the wave phase is given by

$$\Phi(t) = 2\pi f_o t + \pi \dot{f}_o t^2 + \varphi_o - \Phi_D(t). \quad (\text{A2})$$

Here f_o is the initial gravitational wave frequency, \dot{f}_o is the initial frequency derivative, and $A_{+,\times}$ are the polarization amplitudes given in Eq. (3). The Doppler modulation of the signal is given by

$$\Phi_D(t) \simeq \frac{2\pi f_o}{c} \hat{k} \cdot \mathbf{x}_i(t), \quad (\text{A3})$$

where we have neglected the small correction due to the frequency evolution \dot{f}_o . The antenna beam pattern functions $F^{+,\times}(t)$ describe LISA's time varying sensitivity to each polarization and are given by

$$F^+(t) = \frac{1}{2}(\cos(2\psi)D^+(t) - \sin(2\psi)D^\times(t)) \quad (\text{A4a})$$

$$F^\times(t) = \frac{1}{2}(\sin(2\psi)D^+(t) + \cos(2\psi)D^\times(t)), \quad (\text{A4b})$$

where the two-arm detector response functions are defined as

$$D^+(t) \equiv d_{ij}^+ \mathcal{T}_{ij}(t, f_{gw}) - d_{ik}^+ \mathcal{T}_{ik}(t, f_{gw}) \quad (\text{A5a})$$

$$D^\times(t) \equiv d_{ij}^\times \mathcal{T}_{ij}(t, f_{gw}) - d_{ik}^\times \mathcal{T}_{ik}(t, f_{gw}) \quad (\text{A5b})$$

with

$$d_{ij}^+(t) \equiv (\hat{r}_{ij}(t) \otimes \hat{r}_{ij}(t)): \mathbf{e}^+ \quad (\text{A6a})$$

$$d_{ij}^\times(t) \equiv (\hat{r}_{ij}(t) \otimes \hat{r}_{ij}(t)): \mathbf{e}^\times. \quad (\text{A6b})$$

The colon denotes a double contraction, $\mathbf{x}: \mathbf{y} = x^{ab}y_{ab}$, with repeated indices implying a summation, $\hat{r}_{ij}(t)$ is a unit vector that points from spacecraft i to spacecraft j , and $\mathcal{T}_{ij}(t, f_{gw})$ is the round-trip transfer function for the arm connecting the i and j spacecraft,

$$\begin{aligned} \mathcal{T}_{ij}(t, f) = & \frac{1}{2} \left[\text{sinc}\left(\frac{f}{2f_*}(1 - \hat{k} \cdot \hat{r}_{ij}(t))\right) \right. \\ & \times \exp\left(-i\frac{f}{2f_*}(3 + \hat{k} \cdot \hat{r}_{ij}(t))\right) \\ & + \text{sinc}\left(\frac{f}{2f_*}(1 + \hat{k} \cdot \hat{r}_{ij}(t))\right) \\ & \left. \times \exp\left(-i\frac{f}{2f_*}(1 + \hat{k} \cdot \hat{r}_{ij}(t))\right) \right]. \quad (\text{A7}) \end{aligned}$$

The quantity $f_* \equiv c/2\pi L$ is referred to as the transfer frequency, which for LISA ($L = 5 \times 10^6$ km) has a value of 9.54 mHz. The transfer frequency is approximately the point at which a gravitational wave will “fit inside” the detector arms.

The polarization basis tensors are expressed in terms of two orthonormal unit vectors,

$$\mathbf{e}^+ = \hat{u} \otimes \hat{u} - \hat{v} \otimes \hat{v} \quad (\text{A8a})$$

$$\mathbf{e}^\times = \hat{u} \otimes \hat{v} + \hat{v} \otimes \hat{u}. \quad (\text{A8b})$$

The unit vectors \hat{u} and \hat{v} , along with the propagation direction of the gravitational wave, \hat{k} , form an orthonormal triad, which may be expressed as functions of the source location on the celestial sphere (θ, ϕ),

$$\hat{u} = \cos(\theta) \cos(\phi) \hat{x} + \cos(\theta) \sin(\phi) \hat{y} - \sin(\theta) \hat{z} \quad (\text{A9a})$$

$$\hat{v} = \sin(\phi) \hat{x} - \cos(\phi) \hat{y} \quad (\text{A9b})$$

$$\hat{k} = -\sin(\theta) \cos(\phi) \hat{x} - \sin(\theta) \sin(\phi) \hat{y} - \cos(\theta) \hat{z}. \quad (\text{A9c})$$

To calculate the unit vectors $\hat{r}_{ij}(t)$, we use the spacecraft coordinates given by [24],

$$x(t) = R \cos(\alpha) + \frac{1}{2}\varepsilon R(\cos(2\alpha - \beta) - 3 \cos(\beta)) \quad (\text{A10a})$$

$$y(t) = R \sin(\alpha) + \frac{1}{2}\varepsilon R(\sin(2\alpha - \beta) - 3 \sin(\beta)) \quad (\text{A10b})$$

$$z(t) = -\sqrt{3}\varepsilon R \cos(\alpha - \beta). \quad (\text{A10c})$$

In the above $R = 1$ AU is the orbital radius of the guiding center, ε is the orbital eccentricity, $\alpha \equiv 2\pi f_m t + \kappa$ is the orbital phase of the guiding center, $f_m = 1/\text{year}$ is the modulation frequency, and $\beta \equiv 2\pi(n-1)/3 + \lambda$ ($n = 1, 2, 3$) is the relative phase of the spacecraft within the constellation. The parameters κ and λ give the initial ecliptic longitude and orientation of the constellation, respectively. Note that to linear order in the eccentricity, which is the order we work to, the triangular formation is rigid with arm lengths given by $L = 2\sqrt{3}\varepsilon R$.

Equation (A1), and the relationships that follow it, represent the *Rigid Adiabatic Approximation* described in [17]. An important property of the approximation is that it is implemented in the time domain. To properly model sources with frequencies up to 10 mHz requires a minimum of $\sim 10^6$ data points for an observational period of

one year. The computational cost of simulating the response for over 10^7 sources in the time domain is prohibitive.

A desirable alternative is to work directly in the frequency domain. The advantage of doing so is that the number of relevant Fourier coefficients is small. Here the concept of “relevant” are those coefficients that contain a high percentage ($\sim 98\%$) of the spectral power. For reference, a moderate signal-to-noise ratio source at 10 mHz, observed for one year, will spread across 65 frequency bins. It is possible to derive an analytic expression for the Fourier transform of the time domain signal, Eq. (A1). The calculation has four steps. First, the amplitude and frequency modulations are decomposed into harmonics of the detector’s orbital frequency f_m . Second, the frequency evolution term, $\exp(\pi i \dot{f}_o t^2)$, is Fourier transformed. Third, the product of the orbital harmonics and the barycenter wave function $\exp(2\pi i f_o t)$ are Fourier transformed, yielding a Fourier series whose coefficients are products of the harmonic amplitudes and the cardinal sine function. Finally, the Fourier series from steps two and three are convolved to give the complete finite time Fourier transform of the time domain signal. Our calculation generalizes the expression derived by [9] to allow for arbitrary observation times, chirping sources, and the effect of the instrument transfer functions.

The first step in the calculation relies on the fact that the functions $F^+(t)$, $F^\times(t)$, and $\Phi_D(t)$ owe their time variation to the orbital motion of the detector. Thus we may decompose each of these functions into harmonics of the orbital frequency f_m ,

$$F^+(t) = \sum_n p_n e^{2\pi i n f_m t} \quad (\text{A11a})$$

$$F^\times(t) = \sum_n c_n e^{2\pi i n f_m t} \quad (\text{A11b})$$

$$e^{i\Phi_D(t)} = \sum_n d_n e^{2\pi i n f_m t}. \quad (\text{A11c})$$

The coefficients d_n are given by the Jacobi-Anger expansion,

$$d_n = J_n(2\pi f(R/c) \sin\theta) e^{in(\pi/2 - \phi)}, \quad (\text{A12})$$

where J_n is the Bessel function of the first kind of order n . Deriving expressions for p_n and c_n is complicated by the transfer functions that appear in Eq. (A5). While it is possible to perform the harmonic decomposition exactly using the Jacobi-Anger expansion, a simpler approach is to Taylor expand the transfer functions in powers of f/f_* then decompose each term into orbital harmonics. For our current needs a second order expansion is sufficient,

$$\begin{aligned} \mathcal{T}_{ij}(t, f) &= 1 - i(2 + \hat{k} \cdot \hat{r}_{ij}(t)) \left(\frac{f}{2f_*} \right) \\ &\quad - \frac{1}{2}(4 + 3(2 + \hat{k} \cdot \hat{r}_{ij}(t)) + (2 + \hat{k} \cdot \hat{r}_{ij}(t))^2) \\ &\quad \times \left(\frac{f}{2f_*} \right)^2 + \mathcal{O}\left(\frac{f}{2f_*} \right)^3. \end{aligned} \quad (\text{A13})$$

We can now reexpress \mathcal{T}_{ij} , d_{ij}^+ , and d_{ij}^\times in terms of orbital harmonics:

$$\begin{aligned} \mathcal{T}_{ij}(t, f) &= \sum_{n=-4}^4 \tilde{\mathcal{T}}_{ij,n} e^{2\pi i n f_m t} \\ d_{ij}^+(t, f) &= \sum_{n=-4}^4 \tilde{d}_{ij,n}^+ e^{2\pi i n f_m t} \\ d_{ij}^\times(t, f) &= \sum_{n=-4}^4 \tilde{d}_{ij,n}^\times e^{2\pi i n f_m t}. \end{aligned} \quad (\text{A14})$$

Convoluting these expansions yields

$$p_n = \sum_{l=-4}^4 \sum_{m=-4}^4 (\tilde{d}_{ij,l}^+ \tilde{\mathcal{T}}_{ij,m} - \tilde{d}_{ik,l}^+ \tilde{\mathcal{T}}_{ik,m}) \quad (\text{A15a})$$

$$c_n = \sum_{l=-4}^4 \sum_{m=-4}^4 (\tilde{d}_{ij,l}^\times \tilde{\mathcal{T}}_{ij,m} - \tilde{d}_{ik,l}^\times \tilde{\mathcal{T}}_{ik,m}), \quad (\text{A15b})$$

where $n = l + m$. The range of the sums in the above harmonic decomposition can be traced to the functional form of the $\hat{r}_{ij}(t)$ unit vectors. From Eq. (A10) we see that the harmonic decomposition of $\hat{r}_{ij}(t)$ involves a sum from -2 to 2 . The one-arm detector response functions and the expanded transfer functions are each a function of \hat{r}^2 and, therefore, their decompositions range from -4 to 4 .

The second step is to Fourier transform the frequency evolution term, which yields Fourier coefficients q_n that can be expressed in terms of error functions of a complex

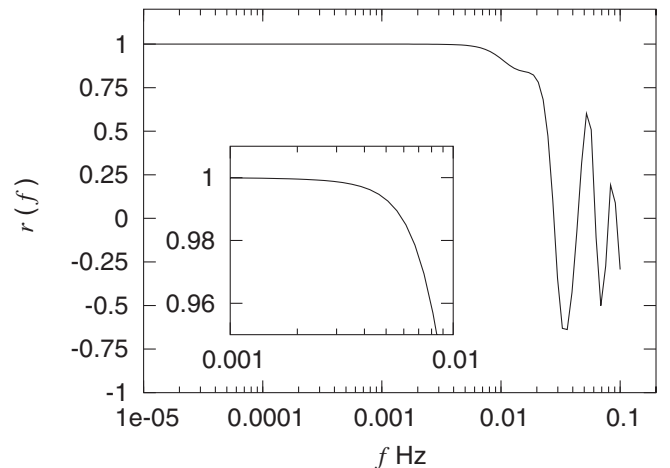


FIG. 14. The correlation between the *Extended Low Frequency Approximation* and the *Rigid Adiabatic Approximation*.

argument. The third step is to Fourier transform the remaining terms over the finite observation time T which has the effect of introducing the cardinal sine function, $\text{sinc}(x) \equiv \sin(x)/x$. Putting everything together we have

$$s_j = \frac{1}{2} e^{i\varphi_0} \sum_k q_k \sum_l \text{sinc}(x_{lm}) e^{ix_{lm}} \sum_n (A_+ p_n + e^{i3\pi/2} A_\times c_n) \times \sum_p d_p, \quad (\text{A16})$$

where $x_{lm} = \pi(lf_m + f_0 T - m)$, $j = k + l$ and $m = n + p$.

To test the range of validity for the new approximation, referred to as the *Extended Low Frequency Approximation* (ELF), we calculated a normalized correlation between the new approximation and the *Rigid Adiabatic Approximation* (RA),

$$r(f) = \frac{\langle s_{\text{RA}}(f) | s_{\text{ELF}}(f) \rangle}{\sqrt{\langle s_{\text{RA}}^2(f) \rangle \langle s_{\text{ELF}}^2(f) \rangle}}. \quad (\text{A17})$$

The rigid adiabatic adequately describes LISA's response up to ~ 0.3 Hz [17] making it a valid benchmark to compare the new approximation against. Figure 14 shows the correlation between the two approximations for a randomly selected binary whose masses, sky location, etc. were held fixed while the correlation was tested at different frequencies. To safely apply the *Extended Low Frequency Approximation*, in our analysis we use a cutoff of 7 mHz as the trigger point for where we switched to the slower *Rigid Adiabatic Approximation*. This allows for quick and accurate frequency domain modeling for all but ~ 100 sources in our galactic simulations.

-
- [1] P. L. Bender *et al.*, LISA Pre-Phase A Report, 1998
- [2] C. R. Evans, I. Iben, and L. Smarr, *Astrophys. J.* **323**, 129 (1987).
- [3] D. Hils, P. L. Bender, and R. F. Webbink, *Astrophys. J.* **360**, 75 (1990).
- [4] P. L. Bender and D. Hils, *Classical Quantum Gravity* **14**, 1439 (1997).
- [5] K. A. Postnov and M. E. Prokhorov, *Astrophys. J.* **494**, 674 (1998).
- [6] G. Nelemans, L. R. Yungelson, and S. F. Portegies Zwart, *Astron. Astrophys.* **375**, 890 (2001).
- [7] J. Crowder and N. J. Cornish, *Phys. Rev. D* **70**, 082004 (2004).
- [8] G. Nelemans, L. R. Yungelson, and S. F. Portegies Zwart, *Mon. Not. R. Astron. Soc.* **349**, 181 (2004).
- [9] N. J. Cornish and S. L. Larson, *Phys. Rev. D* **67**, 103001 (2003).
- [10] <http://astrogravs.gsfc.nasa.gov/docs/mlda/>
- [11] L. Barack and C. Cutler *Phys. Rev. D* **70**, 122002 (2004).
- [12] M. J. Benacquista, J. DeGoes, and D. Lunder, *Classical Quantum Gravity* **21**, S509 (2004).
- [13] J. A. Edlund, M. Tinto, A. Królak, and G. Nelemans, *Phys. Rev. D* **71**, 122003 (2005).
- [14] D. H. Douglass and V. B. Braginsky, in *General Relativity: An Einstein Centenary Survey*, edited by S. W. Hawking and W. Israel (Cambridge University Press, Cambridge, England, 1979), p. 90.
- [15] W. H. Press and K. S. Thorne, *Annu. Rev. Astron. Astrophys.* **10**, 335 (1972).
- [16] K. Danzmann and A. Rüdiger, *Classical Quantum Gravity* **20**, S1 (2003).
- [17] L. J. Rubbo, N. J. Cornish, and O. Poujade, *Phys. Rev. D* **69**, 082003 (2004).
- [18] N. J. Cornish and E. K. Porter, *Classical Quantum Gravity* **22**, S927 (2005).
- [19] E. T. Jaynes, *Probability Theory: The Logic of Science* (Cambridge University Press, Cambridge, England, 1995).
- [20] N. J. Cornish and J. Crowder, *Phys. Rev. D* **72**, 043005 (2005).
- [21] N. J. Cornish, R. W. Hellings, and L. J. Rubbo (unpublished).
- [22] R. Umstätter, N. Christensen, H. Hendry, R. Meyer, V. Simha, J. Veitch, S. Vigeland, and G. Woan, *Phys. Rev. D* **72**, 022001 (2005).
- [23] C. Cutler, *Phys. Rev. D* **57**, 7089 (1998).
- [24] N. J. Cornish and L. J. Rubbo, *Phys. Rev. D* **67**, 022001 (2003).
- [25] S. L. Larson, W. A. Hiscock, and R. W. Hellings, *Phys. Rev. D* **62**, 062001 (2000); <http://www.srl.caltech.edu/shane/sensitivity/MakeCurve.html>